Engineering Fracture Mechanics 147 (2015) 293–305

Contents lists available at ScienceDirect

Engineering Fracture Mechanics

journal homepage: www.elsevier.com/locate/engfracmech

Cohesive zone modeling and calibration for mode I tearing of large ductile plates

P.B. Woelke [a,*], M.D. Shields [a], J.W. Hutchinson [b]

[a] Applied Science and Investigations, Weidlinger Associates, Inc., New York, NY, United States
[b] School of Engineering and Applied Sciences, Harvard University, Cambridge, MA, United States

ARTICLE INFO

Article history:
Received 6 November 2014
Received in revised form 25 February 2015
Accepted 4 March 2015
Available online 16 March 2015

Keywords:
Ductile fracture
Cohesive zone
Crack growth resistance
Structural scale plates and shells
Plate/shell elements

ABSTRACT

This paper focuses on extensive ductile crack growth by modeling a mode I fracture experiment. Solution of this problem, requires structural scale plate/shell finite which cannot resolve the details of the fracture process. Thus, a cohesive zone model, which accounts for the dependence of the cohesive tearing energy on the crack advance is employed. The steady-state cohesive energy is informed by the detailed analysis of necking localization and shear failure, performed with the Gurson model. The structural scale model reveals the partition of the tearing energy into the cohesive energy and the additional plastic dissipation occurring outside the cohesive zone.

1. Introduction

The governing mechanism of ductile fracture in metals is nucleation, growth and coalescence of micro-voids. In stretching of bars or plates of most ductile structural alloys, there is no appreciable porosity in the material until necking localization sets in producing enhanced local stress triaxiality. The increase in tri-axial stress accelerates the void growth and, eventually, causes localization in a shear band and coalescence into a crack [5,13]. The plastic strains inside the neck can reach high levels (on the order of ~100% measured by the grain width reduction [6]) which are usually much larger than strains outside the neck. To accurately capture neck development and progressive damage development within the neck, a detailed numerical analysis is necessary with micromechanically motivated constitutive models, such as the Gurson model [8] and its subsequent modifications [10,20,21], the Perzyna model [7,14], or the Rousselier model [16]. While these micromechanical approaches can reproduce the details of the deformation and plastic dissipation in the fracture process zone, including details such as the cup-cone fracture mode, they require very small element sizes, on the order of void spacing, as emphasized by Xue et al. [32]. This level of resolution is computationally expensive and only feasible for small scale geometries such as coupon test samples. The fact that it is not feasible to use micro-mechanically based constitutive models is a significant handicap for engineers attempting to quantify the response of large-scale structures such as ships, aircraft, and automobiles to extreme loading conditions leading to component-level fracture and failure. Generally, large structures must be analyzed using plate/shell elements with characteristic in-plane lengths larger than the plate thickness.

The present study is specifically concerned with modeling mode I ductile tearing of large sheet metal components such as those found on a ship, an automobile or an aircraft. The large scale of the problem requires large plate/shell finite elements

* Corresponding author. Tel.: +1 212 367 2983.
E-mail address: woelke@wai.com (P.B. Woelke).

http://dx.doi.org/10.1016/j.engfracmech.2015.03.015
0013-7944/

Nomenclature

A_0	initial undeformed cross-sectional area of a tensile coupon
d	overall elongation of the detailed neck model simulated using shear modified Gurson model
D	void spacing in the dominant void population
E	elastic modulus
F	applied force for the detailed neck model simulated using shear modified Gurson model
K	elastic stress intensity factor
$K_R(\Delta a)$	crack growth resistance in small scale yielding under monotonic load
K_{IC}	plane strain mode I toughness – stress based
K_C	plane stress toughness
L	initial specimen length of a tensile coupon
N	Considere condition strain at the necking onset; material power law hardening exponent
P	applied force in large scale fracture model
R_P	plastic zone size
t	plate thickness
T	nominal cohesive traction
T_{max}	maximum cohesive traction
$\widehat{T}$	peak cohesive traction
α	steady-state crack growth coefficient for cohesive energy/area
β	plane strain toughness coefficient
Γ	cohesive energy = work/area required to separate the plate after the onset of necking
Γ_{I}	work/area dissipated in necking
Γ_{II}	work/area dissipated in shear localization
Γ_{IC}	plane strain mode I toughness – energy based
$\Gamma_{steady\text{-}state}$	steady state energy/area
$\Gamma_{SSY}(\Delta a)$	crack growth resistance in small-scale yielding
δ	cohesive separation within the neck region
δ_1, δ_2	cohesive traction–separation shape parameters
δ_{max}	maximum separation across the neck
Δ	crosshead displacement in large scale plate model
Δa	crack advance in small scale yielding
Δx	distance ahead of the pre-crack
ε	strain
ε_{log}	logarithmic strain
ε_0	strain at yield
ν	Poisson's ratio
σ	true stress
σ_M	true stress governing flow of the damage-free base material (matrix material) in the Gurson model
σ_U	ultimate stress
σ_y	yield stress

with a minimum in-plane dimension limited by plate thickness. In this paper, crack growth resistance is modeled starting from initiation from a pre-crack through extensive propagation. Standard shell elements cannot capture the details of necking localization and subsequent micro-mechanical damage and fracture. The complicated behavior beyond the onset of necking leading to failure can be addressed in several ways. In this paper, a cohesive zone is used to represent the sequence of failure processes. Similar efforts for both ductile and brittle materials have been undertaken by other authors [2,4,9,17,31]. Simonsen and Törnqvist [18] employed a critical plastic strain criterion to advance the crack tip, demonstrating how the critical strain must depend on element size when calibrated against experiment. In each approach, the sequence of failure processes is subsumed within either the cohesive zone or the calibrated critical strain. Another approach [24–28,30] employs special shell elements allowing for damage and softening in a phenomenological way to generate the effective non-linear response of the structural components. A recent study by the present authors [29] compared the use of these special elements in plate tearing simulations with an approach based on a cohesive zone. Similar efforts have been recently undertaken by other authors [1,18,19].

The present approach, which is directed to tearing of plates under large scale plastic yielding conditions, has parallels with an early simulation of mode I crack growth under small scale yielding plane strain conditions by Tvergaard and Hutchinson [22]. Those authors embedded a cohesive zone imbued with a peak strength and cohesive energy within a finite element representation of the surrounding elastic–plastic field. Crack growth resistance was computed under monotonically

increasing load from the onset of growth until the approach to steady-state advance. The model was able to partition the total work of fracture into the work of the fracture processes, represented by the cohesive zone, and the plastic work dissipated in the surrounding field. As already noted, in this paper, plane stress elements with in-plane size larger than the plate thickness will be employed along with a cohesive zone model calibrated to capture localization and fracture processes at the scale of the plate thickness and below.

As background, the paper begins in Section 2 with a brief discussion of the difference between mode I crack growth resistance in plane stress small scale yielding and that in plane strain. Then, in Section 3 recent work on the steady-state tearing of large plates is reviewed to provide insight into the specification of the cohesive zone. In Section 4, the necessity of allowing for a dependence of the cohesive fracture energy on crack advance is highlighted, reflecting the role of changing stress triaxiality and the development of necking localization ahead of the crack tip as the crack advances from a pre-crack. Section 4 discusses the experimental results used as a basis for model calibration and verification, as well as the computational model. Full details of the model calibration procedure are provided in Section 5, followed by a review and interpretation of the simulation results. The cohesive zone developed for the particular plate material and thickness are used to compute the tearing resistance behavior for the plate under small scale yielding conditions in Section 6, providing insights into the relation of tearing resistance to the cohesive separation energy. Conclusions and suggestions for further work are given in Section 7.

2. Mode I crack growth resistance in small scale yielding: plane stress versus plane strain

Although the central problem to be addressed in this paper is the mode I tearing of a plate under large scale plastic yielding conditions, it is useful to begin by considering mode I crack growth in ductile alloys under small scale yielding conditions and to contrast the behavior in plane strain with that in plane stress. These considerations provide insights into the formulation of the cohesive zone used in the mode I plate tearing analysis, and they give background to the computation of the small scale yielding resistance curve for the calibrated plate material.

In plane strain, small scale yielding requires the crack tip plastic zone to be small compared to both the overall crack length (or ligament length) and the thickness of the specimen or plate. In plane stress applications, the requirement of small scale yielding only requires the plastic zone to be small compared to the overall crack length and other relevant in-plane lengths. In plane stress, the plastic zone will often be much larger than the plate thickness. In each case, small scale yielding implies that the elastic stress intensity factor, K, characterizes the intensity of the applied loads experienced by the crack tip and plastic zone surrounding it. Crack growth resistance in small scale yielding under monotonically applied load is characterized by $K_R(\Delta a)$ where Δa is the crack tip advance from an initial pre-crack. Qualitative sketches of $K_R(\Delta a)$ for plane strain and plane stress are presented in Fig. 1.

In plane strain, growth initiates at $K_R = K_{Ic}$, given a sufficiently sharp pre-crack. Even modestly tough materials display some crack grow resistance such that the stress intensity required to advance the crack increases with Δa. Steady-state resistance is attained after the crack has advanced on the order of the plane strain plastic zone size, $R_p \cong (K_{Ic}/\sigma_y)^2/10$. For very tough materials, $(K_R)_{steady\text{-}state}$ can be much larger than K_{Ic}. Quantitative results for resistance curve behavior such as that depicted in Fig. 1a have been computed in [22] based on a plane strain model that imbeds a cohesive zone to represent the fracture process within a finite element representation of the surrounding plastic zone and outer elastic field.

The behavior in plane stress depicted in Fig. 1b is qualitatively similar, but the underlying mechanics is distinctly different. For a plate whose thickness, t does not satisfy $t \gg R_p$, the onset of crack growth occurs at K_C. Except for exceedingly thin plates such as foils, $K_C > K_{Ic}$ due to lower stress triaxiality at the crack tip than in plane strain. The initial stage of advance, persisting for a distance of at least several plate thicknesses, is complicated and highly three-dimensional. The crack usually begins to advance at the center of the crack front where the triaxiality is the highest and lags behind near the surfaces. As the applied stress intensity factor increases and the crack tip advances, a neck in the plate begins to form ahead of

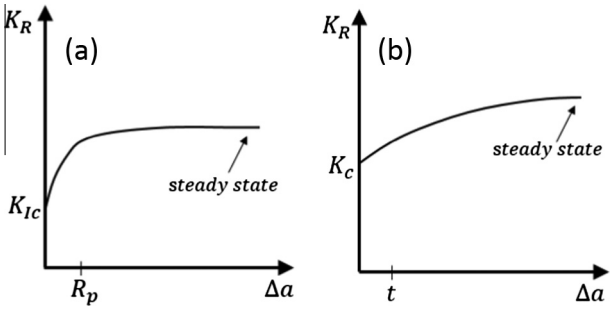

Fig. 1. Qualitative features of mode I crack growth resistance, $K_R(\Delta a)$, for ductile alloys in small scale yielding in plane strain (a) and plane stress (b). In plane strain, steady-state toughness is attained after a crack advance, Δa, of several times the plastic zone size at initiation, R_p. In plane stress, attainment of steady-state toughness requires a crack advance that is at least several times the plate thickness, t, after the necking region advancing ahead of the tip becomes fully developed.

the tip. As the neck develops, shear localization subsequently occurs within the neck oriented at roughly 45° to the plate surfaces, finally giving rise to a slant crack. Steady-state, with a neck advancing ahead of the tip, is attained after the crack has passed through this initial stage. The plane stress steady-state toughness of a ductile alloy can be very large compared to K_C due primarily to the large plastic dissipation in the neck, as elucidated in the next section. The features just described must be reflected in any cohesive zone model of plate tearing.

3. Energy dissipation in mode I steady-state tearing of a plate

Consider mode I tearing of a large ductile plate with a long crack that has advanced sufficiently such that the steady-state conditions depicted in Fig. 2 are attained. Once the onset of necking sets in ahead of the crack (Fig. 2a), the subsequent deformation within the neck occurs under essentially plane strain-like conditions with almost no additional in-plane straining taking place in the direction parallel to the crack. The sequence of deformation stages, (a)–(d), depicted in Fig. 2 have been analyzed in [12]. Aspects of that study relevant to the prescription of the traction–separation relation of the cohesive zone for tearing of large plates will now be summarized.

The deformation sequence depicted in Fig. 2 was modeled by the 2-dimensional plane strain problem indicated in the insert of Fig. 3. The material was represented by the shear-modified Gurson model [10], allowing a detailed analysis of the fracture process from the onset of necking, through thinning and shear localization. In [12], the undamaged material input has power law hardening with a uniaxial true stress versus logarithmic strain given by:

$$\varepsilon_{log} = \begin{cases} \frac{\sigma_M}{E}, & \sigma_M < \sigma_Y \\ \frac{\sigma_Y}{E}\left(\frac{\sigma_M}{\sigma_Y}\right)^{\frac{1}{N}}, & \sigma_M \geqslant \sigma_Y \end{cases} \tag{1}$$

Fig. 3 presents a representative example of the normalized force–displacement relationship [12]. Necking begins at the Considere condition corresponding to a maximum nominal traction, and attained at the strain $\varepsilon = N$:

$$\frac{T_{max}}{\sigma_Y} = \frac{2}{\sqrt{3}}\left(\frac{2}{\sqrt{3}}\frac{NE}{\sigma_Y}\right)^N e^{-N} \tag{2}$$

After the onset of necking, plastic deformation is confined to the neck region. Void damage within the neck grows until conditions are reached when further localization occurs in the form of a shear band extending across the central region of the neck at an angle $\cong 45°$ to the tensile direction. Prior to shear band formation plastic deformation occurs throughout the neck, but once the shear band forms plastic deformation is largely localized within a very narrow band resulting in the precipitous drop in the load-elongation behavior seen in Fig. 3. Shear fracture processes inside the band give rise to final separation during this stage (Fig. 2d).

The aspects of the traction–elongation behavior in Fig. 3 relevant to the task in this paper are as follows. Plane stress finite elements whose in-plane dimensions are larger than the thickness of the plate can accurately represent behavior prior to the onset of necking, but they are incapable of resolving the deformation in the neck and in the shear band. Thus, the traction–displacement relation of the cohesive zone must represent the behavior beyond the maximum traction, as extracted from

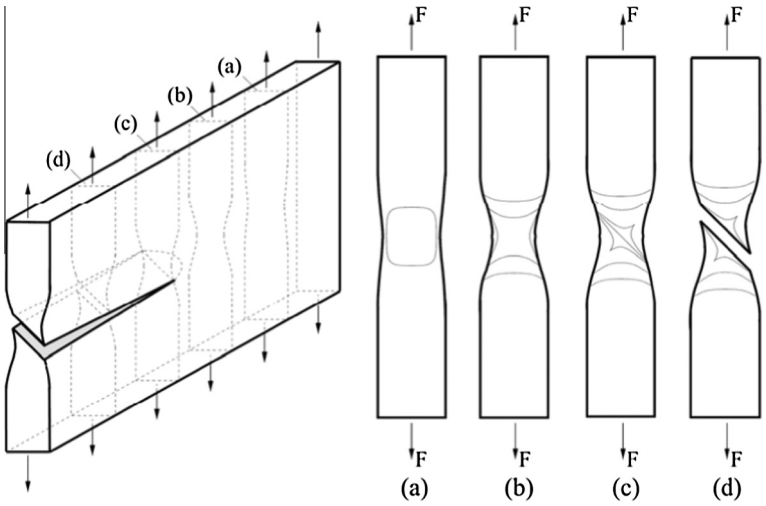

Fig. 2. Sequential fracture process under steady-state crack advance in ductile plate subject to mode I loading: (a) onset of local necking well ahead of the tip, (b) well developed neck nearer the tip, (c) shear localization within the neck and (d) slant failure at the tip. Taken from [12].

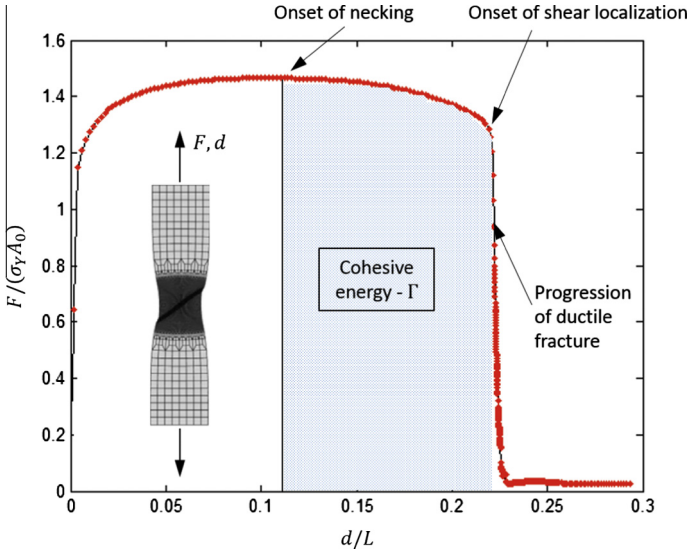

Fig. 3. Representative normalized force–elongation curve for steady-state tearing of ductile structural alloy obtained using the shear modified Gurson material model. The quantities σ_Y, A_0 and L denote the yield stress, initial cross-sectional area, and initial length, respectively, of the undeformed section while F and d are the force and overall elongation. Details of the specification of the material model are given in [12].

Fig. 3 and presented in Fig. 4. In Fig. 4, the vertical axis is the nominal traction (the force per original area) divided by the yield stress T/σ_Y and the horizontal axis is the separation across the neck region occurring after the onset of necking normalized by the plate thickness, δ/t. The area under this curve, Γ, is the work/area required to separate the plate after the onset of necking. This is the cohesive energy/area that must be accounted for by the cohesive zone when steady-state has been attained. An important observation evident in Fig. 4 is that the energy dissipated in the necking process prior to shear localization, Γ_{I}, is usually much greater than that dissipated in shear localization and fracture, Γ_{II}. The behavior illustrated in Figs. 3 and 4 is representative of many relatively tough ductile alloys. As a consequence, the traction–separation energy of the cohesive zone in plane stress plate tearing is very large after the crack has propagated far enough such that the neck is fully developed. It should be noted that the slope of the equilibrium traction–separation curve in Fig. 4 can become negative for sufficiently narrow shear bands or as the band strength degrades. No attempt is made to capture this level of detail in the cohesive zone representation developed in the present paper. As will be seen shortly, the primary aim of the representation is to capture the energy dissipated in necking to failure, with the slope of the traction–separation curve set by a combination of physical and numerical considerations.

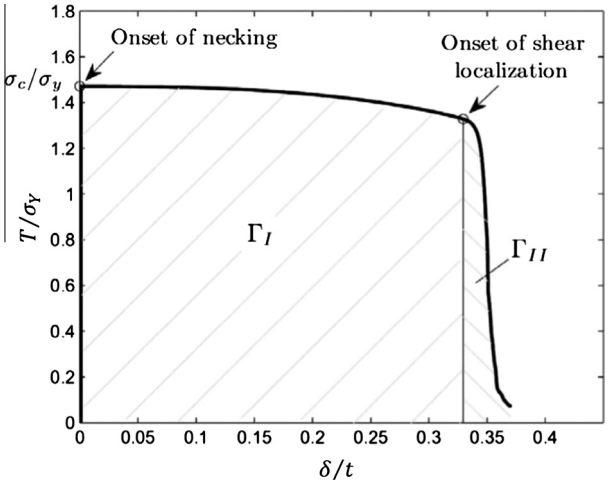

Fig. 4. Representative traction–separation behavior extracted from the force–displacement relationship in Fig. 3 for conditions in which sufficient crack advance has occurred such that a fully developed neck has formed ahead of the crack and steady-state propagation is underway. The separation occurring across the neck region following the onset of necking is denoted by δ. The work/area dissipated in necking is denoted by Γ_{I} while that dissipated in shear localization and shear fracture is denoted by Γ_{II}.

From Fig. 4 one notes that $\Gamma_{steady\text{-}state} \cong T_{max}\delta_{max}$. The maximum separation across the neck, δ_{max}, is proportional to the height of the neck which, in turn, is proportional to the plate thickness, t. Consequently, the steady-state energy/area dissipated can be written as:

$$\Gamma_{steady-state} = \alpha\sigma_Y t \tag{3}$$

where the coefficient α usually lies in the range $0.4 < \alpha < 0.8$ depending on the material hardening exponent and the parameters characterizing the void damage [12]. The important implication for present purposes is that the *steady-state cohesive energy/area is proportional to the plate thickness*. It is interesting to compare (3) with the plane strain mode I toughness expressed in units of energy/area, $\Gamma_{Ic} = (1-\nu^2)K_{Ic}^2/E$. Basic mechanistic models of plane strain toughness [15,23] give:

$$\Gamma_{Ic} = \beta\sigma_Y D \tag{4}$$

where D is the spacing between voids in the dominant void population. The coefficient β is on the order of unity and depends on material properties such as strain hardening and initial void volume fraction. Dominant void spacing is typically tens of microns and seldom more than a hundred microns. It therefore follows from (3) to (4) that the steady-state cohesive energy/area, $\Gamma_{steady\text{-}state}$, of plates with thicknesses larger than a millimeter will be many times the plane strain toughness of the material, Γ_{Ic}. Further, whereas plane strain toughness is a material quantity, the plane strain steady-state cohesive energy/area of a plate depends on the both the material and the plate thickness. As an aside, it is also interesting to note that the above comparison also suggests that the tearing toughness of a thin foil is likely to be less than Γ_{Ic} if its thickness is less than the characteristic void spacing.

4. Cohesive zone characterization for mode I tearing of a plate with an initial pre-crack

In this section, the cohesive zone used in conjunction with plane stress plate (or shell) elements is addressed for analyzing mode I crack advance initiating from a pre-crack in a large scale plate structure. The preceding discussion motivates the necessity of allowing for a cohesive energy/area, $\Gamma(\Delta x)$, that is an increasing function of the distance Δx ahead of the pre-crack tip. Fig. 5 displays $\Gamma(\Delta x)$ as calibrated in the next section for a 10 mm thick Al 5083 H116 plate tested by Simonsen and Törnqvist [18]. For this plate, the steady-state cohesive energy/area (3) is attained when the crack has propagated about seven times the plate thickness. Moreover, it is almost fifty times the value required to initiate crack growth from the blunt pre-crack.

The traction–separation relation, $T(\delta)$, used in this paper is presented in Fig. 6. The peak traction, $\widehat{T}$, and the length parameters, δ_1 and δ_2, determining the shape can be regarded as functions of distance ahead of the pre-crack, Δx. At each Δx, the cohesive energy/area is:

$$\Gamma(\Delta x) = \int_0^{\delta_2} T d\delta = \frac{1}{2}\widehat{T}(\delta_1 + \delta_2) \tag{5}$$

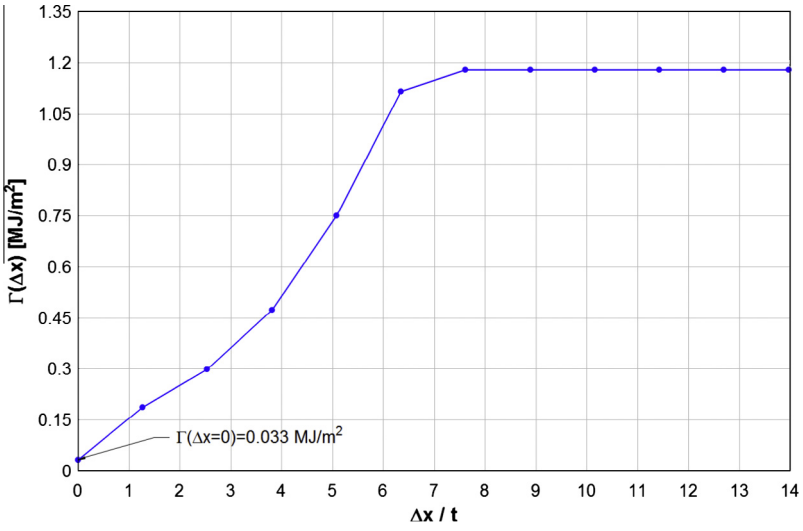

Fig. 5. Variation of the cohesive energy/area of a cohesive zone model for analyzing mode I cracking in initiating from a pre-crack in a large plate when plane stress elements larger than the plate thickness, t, are employed. This particular curve has been calibrated for a 10 mm thick plate of Al 5083 H116 aluminum discussed in Section 5.

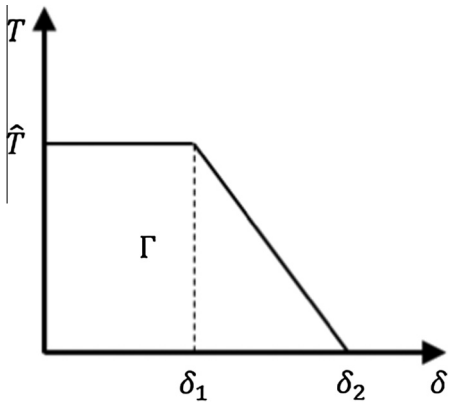

Fig. 6. Form of the traction–separation relation used in this paper with peak traction $\hat{T}$ and shape parameters, δ_1 and δ_2.

Full details of the description for the test plate will be given in the next section. The choice of a separation curve which ramps down to zero traction in a gradual manner such as that in Fig. 6, is deliberate because it avoids computational problems. More abrupt traction drops, such as that in Fig. 4, can give rise to discontinuous crack advancement and to a "stair-stepped" force–displacement curve. Additionally, such a rapid drop in stiffness can cause spurious numerical oscillations ("ringing") in the simulations. These effects can be particularly problematic for analyses conducted with relatively large elements, as is the case here. Thus, the gradual traction fall-off such as that in Fig. 6 is important to the large plate simulations carried out here. Plane strain studies such as those in [22] have indicated that the two most important properties of the separation-law are the peak traction and the energy of separation, with shape details of the traction–separation curve of secondary importance. The present study under plane stress conditions reveals more sensitivity to the details of the shape, as discussed in the next section.

5. Calibration of cohesive zone using load–displacement data for a pre-cracked plate

A detailed investigation of a specific large aluminum plate subjected to Mode I ductile tearing is discussed here. The plate tearing problem was simulated using large scale shell elements with cohesive elements along the crack path. The measured overall force–displacement response is used to calibrate the traction–separation relationship of the cohesive zone discussed in the previous section and its variation with crack advance. First, some details of the experimental test are discussed. Then, the finite element model is prescribed followed by a description of the calibration process.

5.1. Problem description and experimental test results

The problem investigated here is a pre-notched large aluminum AL 5083 H116 plate subjected to mode I tearing, part of a test series on naval-grade plate materials conducted by Simonsen and Törnqvist [18]. The test was conducted by means of a specially designed load frame shown in Fig. 7. The plate dimensions are: height = 806 mm, width = 500 mm, and thickness = 10 mm. A 100 mm initial notch was machined into the plate with a 5 mm diameter hole at the initial tip. The large scale of the frame makes it a unique apparatus for experimental testing of large-scale structural components. A similar load frame has recently been built at the Naval Surface Warfare Center Carderock Division to conduct large-scale experimental tests relevant to the military and civilian shipping industry [11].

The photograph of the tested plate after the crack has propagated almost entire width of the specimen is shown in Fig. 7. The experimental force vs. corrected crosshead displacement, will be discussed in more detail in Section 5.3.

Uniaxial tensile tests for the plate material (Al 5083 H116) in [18] led to a power law hardening true stress vs. logarithmic strain relationship:

$$\sigma = C(\varepsilon_{log} + \varepsilon_0)^N \tag{6}$$

with parameters $C = 550$ MPa, $\varepsilon_0 = 0.01$, and $N = 0.2$. The reported material yield strength and ultimate strength are $\sigma_Y = 245$ MPa,$\sigma_U = 334$ MPa and the elastic modulus is $E = 69$ GPa.

5.2. Finite element model

The finite element model used in the analyses is shown in Fig. 8. The plate was modeled with large quadrilateral shell elements with Mindlin–Reissner kinematics, using the explicit dynamic finite element code EPSA [3,27,28]. Nodal spring-type cohesive elements were used along the crack path. The top and bottom rectangular 'grips' were modeled as rigid bars.

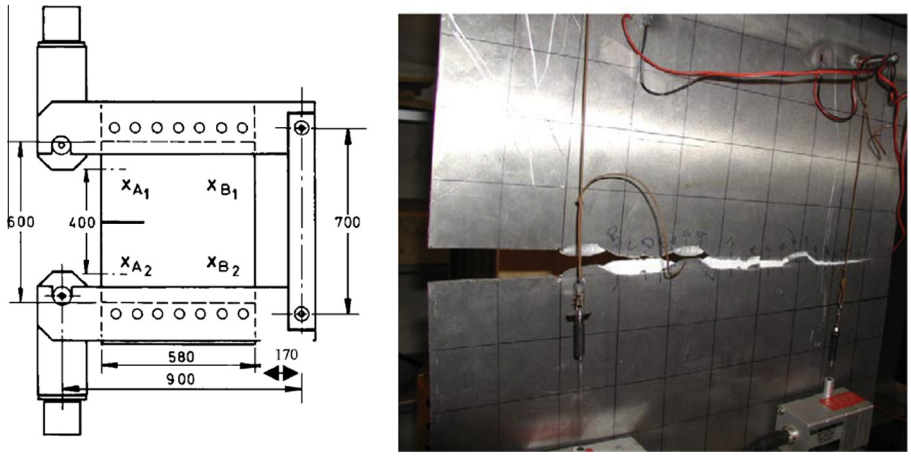

Fig. 7. Experimental load frame and fractured aluminum plate [18].

Points B and B' (Fig. 8) were fixed to prohibit vertical translation. The plate was loaded by applying a constant vertical velocity to nodes A and A' located on the front faces of the grips. Force, P, and displacement, Δ were computed at these nodes for comparison with the experimentally measured quantities.

The power hardening law (6) for Al 5083 H116 was used to represent the material with the parameters reported. A mesh sensitivity study was conducted using three different meshes: 12.7 mm, 25 mm, and 50 mm – resulting in a total of 3400, 768, and 296 total elements respectively. The smallest element size (12.7 mm) was limited by the plate thickness ($t = 10$ mm).

5.3. Cohesive zone calibration

Calibration of the cohesive zone for the large-scale model requires determination of the traction–separation relationship for the individual cohesive elements along the crack path ahead of the pre-crack. As discussed earlier, one must anticipate that the cohesive energy/area will be relatively small for elements immediately ahead of the pre-crack tip and increase toward the steady-state level for elements lying more than several thicknesses ahead of the tip. The measured force–displacement response of the Simonsen and Törnqvist [18] test shown in Fig. 9 will be used to perform the calibration. Systematic procedures for calibrating the position-dependent traction–separation law are not available, and future effort will be needed to develop calibration approaches, including extensions for crack growth under mixed mode loadings. The

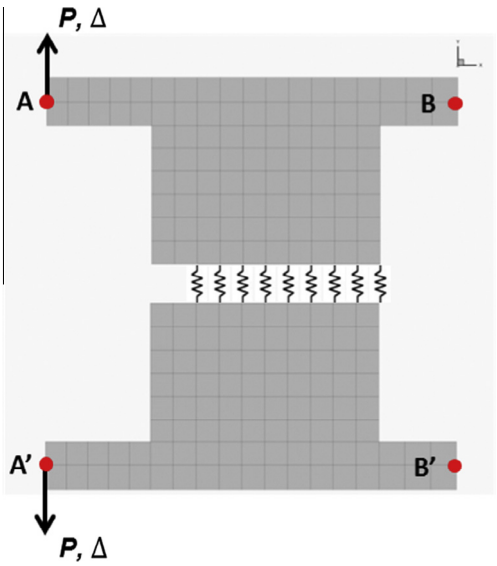

Fig. 8. Finite element representation of the mode I fracture test (50 mm mesh). Vertical translation was fixed at points B and B'.

present approach makes use of the steady-state results presented in Section 3 together with a rather straightforward 'trial and error' procedure.

In the present approach, the peak traction, $\widehat{T}$, is taken to be the maximum traction in (2), $T_{max} = 334$ MPa, and this is assumed to be independent of Δx. The steady-state cohesive energy is taken to be that given in (3) with $\alpha = 0.48, \sigma_y = 245$ MPa and $t = 10$ mm such that $\Gamma_{steady\text{-}state} = 1.175$ MJ/m^2. This choice coincides with the cohesive energy/area of the example in Fig. 4 which, as discussed in Section 3, was computed using the fine scale damage model [12]. Given $\widehat{T} = T_{max}$, it remains to determine $\Gamma(\Delta x)$ and the Δx-distribution of δ_1/δ_2. (By (5), only one of δ_1 and δ_2 is undetermined if $\widehat{T}$ and Γ are known.) In our approach, the first step was to take $\Gamma = \Gamma_{steady\text{-}state}$, and investigate the influence of δ_1/δ_2, both taken independent of Δx. If the only considerations were numerical, the choice $\delta_1/\delta_2 \cong 0$ would provide the best numerical conditioning of the FE calculation for reasons described earlier. However, the actual traction–separation behavior in Fig. 4 has an abrupt fall-off with δ_1/δ_2 only slightly less than unity. Here, we have compromised numerical conditioning and the fact that actual traction–separation behavior in the steady-state regime has the abrupt fall-off.

Tearing simulations using a 12.7 mm mesh were carried out for various values of δ_1/δ_2. With $\delta_1/\delta_2 \cong 1/3$ ($T_{max} = 334$ MPa, $\Gamma(\Delta x) = \Gamma_{steady\text{-}state} = 1.175$ MJ/m^2), the simulated force versus cross-head displacement is the upper curve in Fig. 9. This choice accurately reproduces the measured tearing resistance of the plate after more than 100 mm crack growth (although it significantly overestimates the peak force, as discussed below). By contrast, a simulation with $\delta_1/\delta_2 = 0$ and the same values of T_{max} and $\Gamma_{steady\text{-}state}$ significantly underestimates the tearing resistance after extensive crack growth, as the lower curve in Fig. 9 reveals (further details of this simulation will also be discussed below). The simulated tearing resistance clearly depends on δ_1/δ_2. The initial choice of steady-state cohesive energy based on the results in Section 3, $\Gamma_{steady\text{-}state} = 1.175$ MJ/m^2, was somewhat fortuitous and not necessarily the best choice: had a slightly larger value been chosen, the calibrated value of δ_1/δ_2 would be less than 1/3 and vice versa. Nevertheless, the values $\delta_1/\delta_2 \cong 1/3$, $T_{max} = 334$ MPa, $\Gamma_{steady\text{-}state} = 1.175$ MJ/m^2 will be used to characterize the steady-state limit.

The simulation with an Δx-independent steady-state cohesive energy/area, $\Gamma(\Delta x) = \Gamma_{steady\text{-}state} = 1.175$ MJ/m^2, significantly overestimates peak force, as indicated by the upper curve in Fig. 9. The initial cohesive energy must be lower than the steady-state limit, as already anticipated in the earlier discussion. Thus, it remains to determine the Δx dependence of Γ and δ_1/δ_2 ahead of the pre-crack tip in the approach to the steady-state limit. In the present calibration approach, with a given distribution of δ_1/δ_2, the distribution $\Gamma(\Delta x)$ is determined such that the experimental load–displacement record is reproduced. This is a straightforward sequential process whereby Γ is assigned values element by element ahead of the tip such that the predicted load–displacement curve coincides as closely as possible with the experimental curve as the crack advances element by element. The result of this process is the distribution $\Gamma(\Delta x)$ in Fig. 5 and the companion plot in Fig. 10 showing entire curves of nodal cohesive force versus opening displacement for the 12.7 mm FE mesh. The calibrated value of the cohesive energy at fracture initiation is $\Gamma(\Delta x = 0) = 0.033$ MJ/m^2, which is just above the nominal plane strain toughness of Al5083-H116: $\Gamma_{lc} = 0.027$ MJ/m^2. This indicates that at the notch tip, a near plane strain condition persists. For a plate with increasing thickness, in reference to the plate analyzed here ($t > 10$ mm), these values would converge. For a thinner plate however, the difference would likely increase. Thus, the plane strain toughness could be used as a limiting value for the initial estimate of the cohesive energy/area.

Because the global finite element model utilizes nodal cohesive elements (Fig. 8), the traction–separation relationship must be converted to a nodal cohesive force–displacement relationship. This is accomplished by multiplying the traction–separation relationship by the tributary area of every nodal cohesive element. The peak cohesive force in the first element (at the notch tip) was reduced by ½, because its tributary width is ½ that of the other elements due to the initial notch radius of the pre-crack. The simulated applied force-crosshead displacement with the calibrated cohesive zone is the middle dashed curve in Fig. 9. Steady-state traction–separation is imposed for all elements starting with the seventh cohesive element and beyond corresponding to $\Delta x \cong 70$ mm, approximately 7 times the plate thickness.

The distribution of δ_1/δ_2 for the 12.7 mm mesh in Fig. 10 has been determined by trial and error iteration, but constrained to merge with $\delta_1/\delta_2 = 1/3$ in the steady-state limit. As shown in Fig. 10, $\delta_1/\delta_2 = 0$ was used before reaching the steady-state limit. A different distribution of δ_1/δ_2 would give rise to some change in $\Gamma(\Delta x)$ presented in Fig. 5. In this paper, the importance of an Δx-dependent cohesive traction–separation relation in modeling plate tearing has been highlighted. Further work will be required to derive more systematic approaches to calibration of the traction–separation relationship and to more completely understand conditions needed to render unique distributions of $\widehat{T}$, Γ and δ_1/δ_2.

To emphasize the importance of the choice of δ_1/δ_2, a simulation with $\delta_1/\delta_2 = 0$, $T_{max} = 334$ MPa and $\Gamma(\Delta x)$ given by Fig. 5 has been carried out and is plotted as the lowest curve in Fig. 9. This choice reproduces the initial force-crosshead behavior, almost to the peak force, when the crack advance is less than about 50 mm, as would be expected because the calibrated cohesive zone has $\delta_1/\delta_2 = 0$ for $\Delta x < 50$ mm. For larger crack advance, the predicted applied force falls well below the experimental curve, as discussed earlier.

Fig. 11 presents simulations with three mesh sizes (12.7, 25 and 50 mm), each with the same calibrated cohesive zone traction–separation relation, i.e., with $\Gamma(\Delta x)$ in Fig. 5 and δ_1/δ_2 distributed in the manner shown in Fig. 10 for the 12.7 mm mesh. Relatively little mesh-dependence is evident.

Equivalent strain contours for all three meshes are shown in Fig. 12 at the crosshead displacement of 30 mm when the crack has traversed more than half way across the initial uncracked ligament. The boundary to the light region coincides

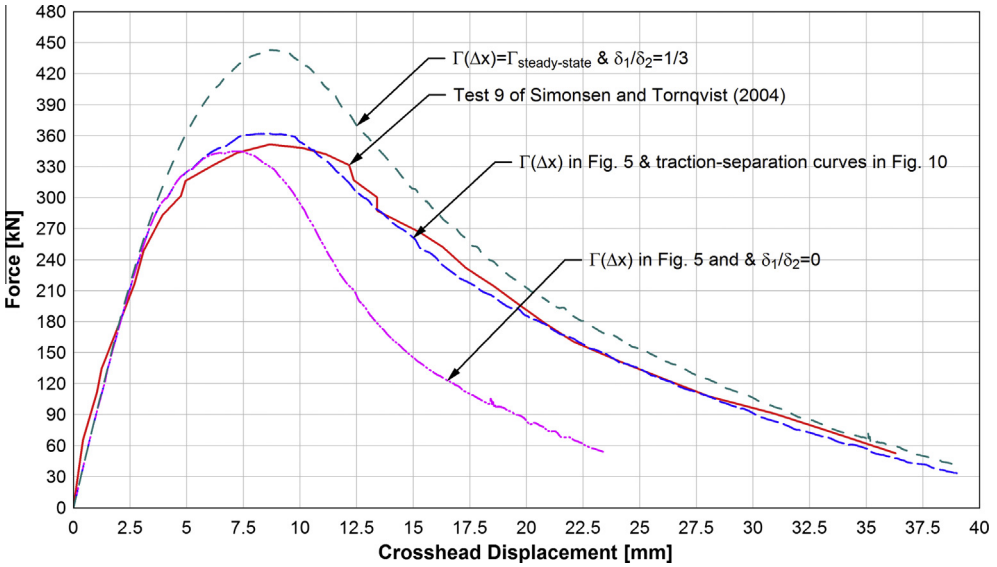

Fig. 9. Applied force vs. crosshead displacement as measured in the test 9 of Simonsen and Törnqvist [18] and the FE models with three cohesive zone choices — upper dashed curve with $\Gamma(\Delta x) = \Gamma_{steady\text{-}state}$ and $\delta_1/\delta_2 = 1/3$; middle curve with $\Gamma(\Delta x)$ in Fig. 5 and traction–separation curves in Fig. 10; lower curve with $\Gamma(\Delta x)$ in Fig. 5 and $\delta_1/\delta_2 = 0$. The FE mesh size is 12.7 mm.

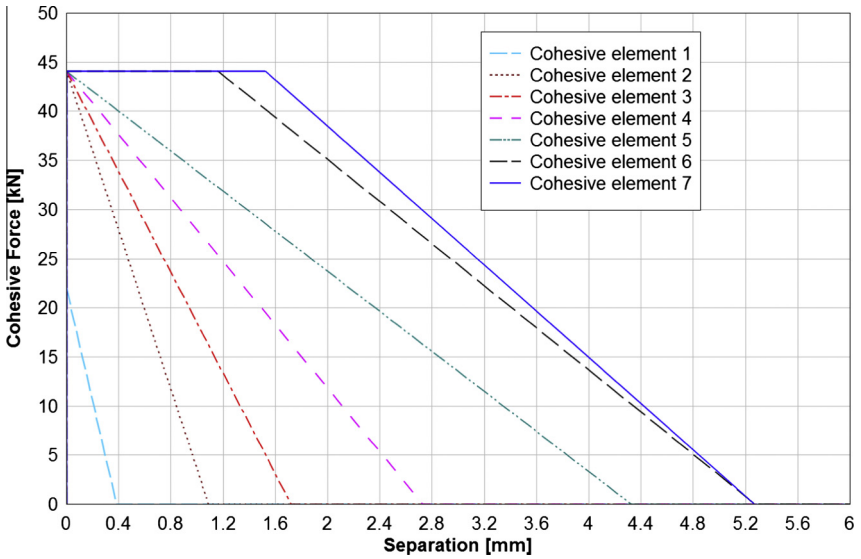

Fig. 10. Cohesive force–displacement relations for nodal cohesive elements – 12.7 mm mesh. The cohesive element 1 is at the initial notch tip. The distribution of $\Gamma(\Delta x)$ is given in Fig. 5.

roughly with the elastic–plastic boundary indicating that extensive plasticity occurs outside the cohesive zone—this is a large scale yielding crack propagation problem. The large scale yielding aspect of the problem is driven home by Fig. 13 where three contributions to the energy input as a function of the applied crosshead displacement have been presented based on the FE simulations: (i) the total energy (the work done by the applied load, which agrees closely with the experiment), (ii) the energy stored and dissipated in cohesive zone, and (iii) the energy dissipated plastically and stored elastically outside the cohesive zone. After the crack has undergone extensive advance most of the energy outside the cohesive zone has been dissipated in plastic deformation. For this plate, even though the cohesive tearing energy of the plate is huge, nevertheless, more than twice the energy is dissipated in plastic deformation outside the cohesive zone than in the cohesive zone. Here, too, these results are insensitive to mesh size. It is apparent that this problem could not be addressed by means of linear elastic fracture mechanics, e.g., small scale yielding.

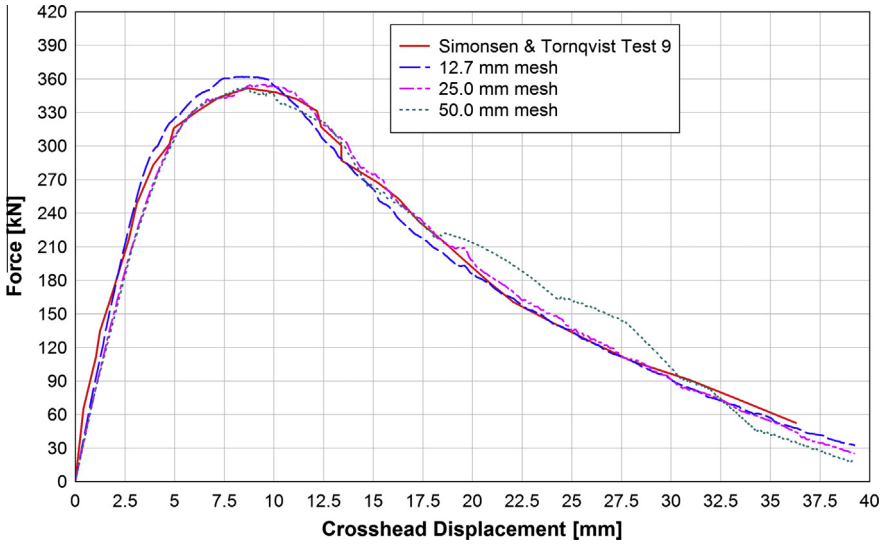

Fig. 11. Applied force vs. crosshead displacement as measured in the experiment and the FE models with three mesh sizes — 12.7, 25.0 and 50.0 mm. The three simulations curve with $\Gamma(\Delta x)$ as the final calibration (Fig. 5) and the traction–separation distribution illustrated for the 12.7 mm mesh in Fig. 10.

6. Relation between small scale yielding crack growth resistance and $\Gamma(\Delta x)$

The test analyzed in the previous section involved large scale plastic yielding. In this section, we compute the crack growth resistance of a plate of the same material (Al 5083 H116) and the same thickness (10 mm) in small scale yielding in plane stress, denoted by $\Gamma_{SSY}(\Delta a)$ with Δa as the crack advance. The same traction–separation relation obtained in Section 5, as specified in Figs. 5 and 10, are employed in the simulation. In particular, the relation between $\Gamma_{SSY}(\Delta a)$ and the cohesive energy/area, $\Gamma(\Delta x)$, given in Fig. 5 will be computed. The finite element model with the 12.7 mm mesh is used and is similar to the one in the previous section except that now the plate size is considerably larger (1.5 m $\times$ 1.5 m) such that the plastic zone is a small fraction of the crack length and the ligament ahead of the crack for the entire range of crack advance considered. To simulate small-scale yielding, tractions associated with the mode I plane stress crack tip fields with amplitude K_I are imposed on the outer boundary of the plate where $\Gamma_{SSY} = K_I^2/E$. The traction–separation law is imposed along the line extending ahead of the crack tip. The small scale yielding crack growth resistance is plotted in Fig. 14 as $\Gamma_{SSY}(\Delta a)/\Gamma_{steadystate}$ versus $\Delta a/t$ where $\Gamma_{steadystate}$ is the steady-state energy/area of the cohesive zone. Included in this figure is the entire x-dependent separation energy of the cohesive zone, $\Gamma(\Delta x)$, from Fig. 5.

The features of the small scale yielding, plane stress tearing resistance are similar to those depicted in Fig. 1b in terms of the stress intensity factor. For this plate material and thickness, steady-state tearing in small scale yielding requires a crack advance of about 15 times the plate thickness, roughly twice the distance ahead of the crack tip at which the cohesive zone becomes x-independent. The difference is due to the plasticity in the plate outside the cohesive zone that develops as the crack advances. In this case, the crack growth tearing resistance in steady-state is more than twice the steady-state cohesive zone separation energy, e.g., 2.7 MJ/m^2 vs. 1.175 MJ/m^2. As noted earlier, this huge tearing resistance is due in part to plastic dissipation in the neck ahead of the crack tip, which constitutes most of the cohesive separation energy, and in part to the plastic dissipation occurring outside the cohesive zone. For this plate material and thickness, those two contributions are roughly equal.

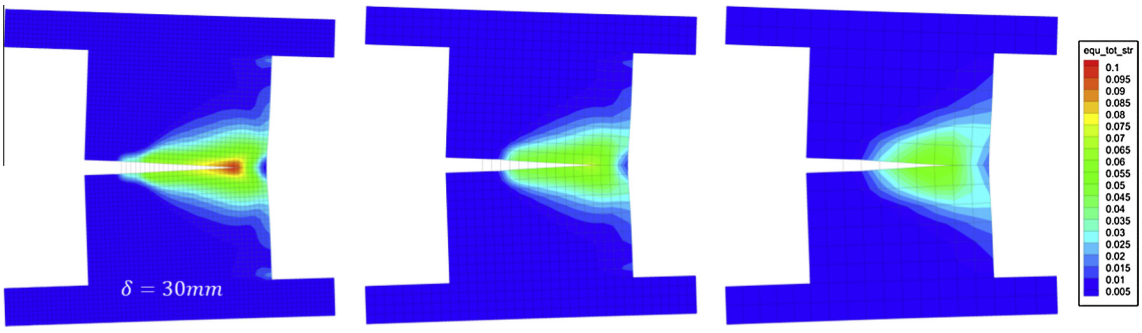

Fig. 12. Equivalent strain contours at a cross-head displacement of 30 mm during fracture for the three different FE meshes considered. The light green region coincides roughly with the extent of the plastic zone.

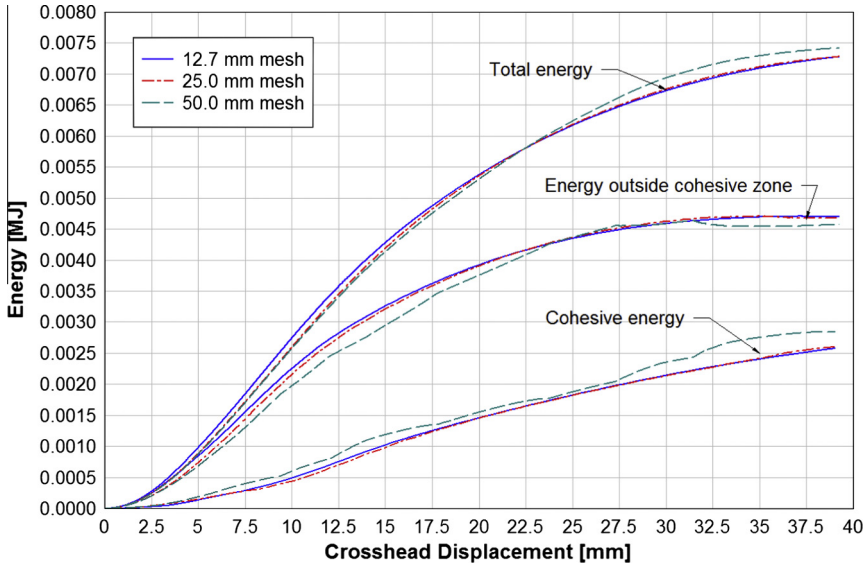

Fig. 13. Computed energy contributions for three meshes for the simulations in Fig. 11: The total energy delivered by the force working through the applied crosshead displacement; the elastic energy and plastic dissipation outside the cohesive zone (in the plate elements); and the energy stored and dissipated in the cohesive zone.

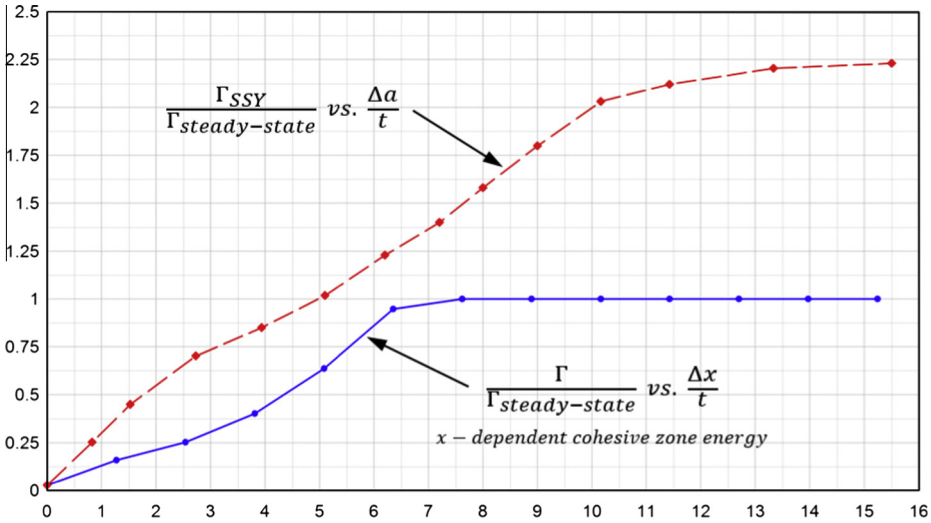

Fig. 14. Normalized small scale yielding crack growth resistance, $\Gamma_{SSY}(\Delta a)/\Gamma_{steady\text{-}state}$, computed for the 10 mm Al 5083 H116 plate using the cohesive separation energy/area, $\Gamma(\Delta x)$, together with the traction–separation distribution in Fig. 10. $\Gamma_{steady\text{-}state}$ is the steady-state separation energy of the cohesive zone.

7. Conclusions and recommendations for further work

In the Introduction, it was emphasized that application of the shell finite element models to ductile fracture problems of practical concern for marine, aerospace, automotive and other industries utilizing large-scale structures requires that the representation of the fine scale fracture processes be subsumed within, for example, a critical fracture strain or, in the case of the present study, a cohesive zone. Calibrating the parameters of the cohesive zone is an essential step of any computational scheme for ductile fracture based on a cohesive zone—a step which has not received the attention it deserves. The calibration process is generally not straightforward especially when it is necessary to account for a position-dependent traction law. In this paper, the calibration employed both inputs from fine scale traction–separation computations and direct fitting to experimental data. We have emphasized that the procedure employed here is neither systematic nor optimal and

that further efforts will be required to refine the calibration procedures. This will be even more important for mixed mode tearing analysis.

The present investigation has demonstrated that a large scale shell finite element model with cohesive zone can be successfully used to capture crack initiation and extensive crack propagation in a ductile plate. The importance of accounting for a dependence of the cohesive zone properties on distance ahead of an initial crack or blunt notch has been highlighted. For tough ductile plates, the development of the maximum, or steady-state, cohesive separation energy requires crack advances of many times the plate thickness — about 7 times the plate thickness in the plate considered. In the early tearing stages before attainment of steady-state, the cohesive energy is much smaller. Most of the cohesive separation energy in steady-state plate tearing is due to plastic dissipation in the neck that develops ahead of the advancing crack tip. For this reason, the steady-state cohesive separation energy scales with the plate thickness. For a plate whose thickness exceeds several millimeters, the steady-state tearing toughness measured in units of energy/area can be orders of magnitude larger than the corresponding plane strain toughness of the material. The specific tearing test modeled in this paper, a 10 mm Al 5083 H116 edge-notched plate tested by Simonsen and Törnqvist [18], reveals that large scale yielding accompanies the tearing with more energy dissipated outside the cohesive zone than within it.

Acknowledgements

The support of the Office of Naval Research: Dr. Paul Hess (Contract No. N00014-10-M-0252) is gratefully acknowledged. The authors also gratefully acknowledge technical assistance of Dr. Ken Nahshon (Naval Surface Warfare Center Carderock) who offered numerous valuable suggestions. Dr. Shields was supported by the National Science Foundation under Grant # EEC-0946363 to the American Society for Engineering Education. Dr. Woelke was partially supported by Weidlinger Associates, Inc. internal research fund.

References

[1] AbuBakar A, Dow RS. Simulation of ship grounding damage using the finite element method. Int J Solids Struct 2013;50(5):623–36.
[2] Anvari M, Scheider I, Thaulow C. Simulation of dynamic ductile crack growth using strain-rate and triaxiality-dependent cohesive elements. Engng Fract Mech 2006;73:2210–28.
[3] Atkatsh RS, Baron ML, Bieniek MP. A finite difference variational method for bending of plates. Comput Struct 1980;11:573–7.
[4] Coureau J-L, Morel S, Dourado N. Cohesive zone model and quasibrittle failure of wood: a new light on the adapted specimen geometries for fracture tests. Engng Fract Mech 2013;109:328–40.
[5] El-Naaman SA, Nielsen KL. Observations on mode I ductile tearing in sheet metals. Eur J Mech A Solids 2013;42:54–62.
[6] Ghahremaninezhad A, Ravi-Chandar K. Ductile failure behavior of polycrystalline Al 6061-T6. Int J Fract 2012;174:177–202.
[7] Glema A, Łodygowski T, Sumelka W, Perzyna P. The numerical analysis of the intrinsic anisotropic microdamage evolution in elasto-viscoplastic solids. Int J Damage Mech 2009;18(3):205–31.
[8] Gurson AL. Continuum theory of ductile rupture by void nucleation and growth – Part I. Yield criteria and flow rules for porous ductile media. J Engng Mater Technol 1977;99:2–15.
[9] Li W, Siegmund T. An analysis of crack growth in thin-sheet metal via cohesive zone model. Engng Fract Mech 2002;69:2073–93.
[10] Nahshon K, Hutchinson JW. Modification of the Gurson model for shear failure. Eur. J. Mech. A/Solids 2008:1–17.
[11] Nahshon K, Hoffman WA, Ullagaddi C. Ductile fracture of large marine aluminum panels. Naval Surface Warfare Center Carderock Division, NSWCCD-66-TR-2013/12.
[12] Nielsen KL, Hutchinson JW. Cohesive traction–separation laws for tearing of ductile metal plates. Int J Impact Engng 2011;48:15–23.
[13] Pardoen T, Hachez F, Marchioni B, Blyth PH, Atkins AG. Mode I fracture of sheet metal. J Mech Phys Solids 2004;52:423–52.
[14] Perzyna P. Constitutive modeling of dissipative solids for postcritical behaviour and fracture. ASME J Engng Mater Technol 1984;106:410–9.
[15] Rice JR, Johnson MA. In: Kanninen MF et al., editors. Inelastic behavior of solids. New York: McGraw-Hill; 1970.
[16] Rousselier G. Ductile fracture models and their potential in local approach of fracture. Nucl Engng Des 1987;105:97–111.
[17] Scheider I, Brocks W. Cohesive elements for thin-walled structures. Comput Mater Sci 2006;37:101–9.
[18] Simonsen BC, Törnqvist R. Experimental and numerical modelling of ductile crack propagation in large-scale shell structures. Mar Struct 2004;17:1–27.
[19] Simonsen BC, Törnqvist R, Lutzen M. A simplified grounding damage prediction method and its application in modern damage stability requirements. Mar Struct 2009;22:62–83.
[20] Tvergaard V. Influence of voids on shear band instabilities under plain strain conditions. Int J Fract 1981;17:389–407.
[21] Tvergaard V. On localization in ductile materials containing spherical voids. Int J Fract 1982;18:237–52.
[22] Tvergaard V, Hutchinson JW. The relation between crack growth resistance and fracture process parameters in elastic-plastic solids. J Mech Phys Solids 1992;40:1377–97.
[23] Tvergaard V, Hutchinson JW. Two mechanisms of ductile fracture: void by void growth versus multiple void interaction. Int J Solids Struct 2002;39:3581–97.
[24] Voyiadjis GZ, Woelke P. General non-linear finite element analysis of thick plates and shells. Int J Solids Struct 2005;43(7-8):2209–42. 1.
[25] Voyiadjis GZ, Woelke P. Elasto–plastic and damage analysis of plates and shells. Springer-Verlag; 2006. 2008.
[26] Woelke P, Abboud N. Modeling fracture in large scale shell structures. J Mech Phys Solids 2012;60(12):2044–63.
[27] Woelke P, Chan KK, Daddazio R, Abboud N, Voyiadjis GZ. Analysis of shear flexible layered isotropic and composite shells by EPSA. Shock Vib 2012;19:459–75.
[28] Woelke P, Chan KK, Daddazio R, Abboud N. Stress-resultant based elasto-viscoplastic thick shell model. Shock Vib 2012;19:477–92.
[29] Woelke P, Shields MD, Abboud NN, Hutchinson JW. Simulations of ductile fracture in the idealized ship grounding scenario using phenomenological damage and cohesive zone models. Comput Mater Sci 2013;80:79–95.
[30] Woelke P, Voyiadjis GZ, Perzyna P. Elasto–plastic finite element analysis of shells with damage due to microvoids. Int J Num Meth Engng 2006;68(3):338–80.
[31] Xu X-P, Needleman A. Numerical simulations of fast crack growth in brittle solids. J Mech Phys Solids 1994;42:1397–434.
[32] Xue Z, Pontin MG, Zok FW, Hutchinson JW. Calibration procedures for a computational model of ductile fracture. Engng Fract Mech 2010;77:492–509.